ADVANCED THEORY AND SIMULATIONS
www.advtheorysimul.com

Fusion of Stacked Nanowires: From Atomistic to Analytical Models

*Harish Devaraj, Md. Naim Jahangir, Zhongwei Gao, Chih-hung Chang, and Rajiv Malhotra**

Fusion of metallic nanowires (NWs) is of increasing interest for fabricating printed devices. Atomistic simulations of inter-NW neck growth during thermal fusion of vertically stacked silver nanowires (NWs) with nonorthogonal axes are performed, a geometric configuration that is commonly seen in applications. High NW rotation during fusion is uncovered surprisingly and found that it accelerates inter-NW neck growth beyond that explainable by conventional geometric arguments. Rotation-regulated surface diffusion and dislocation generation are found to be the culpable mechanisms and are shown to be dominant in distinct regimes of initial NW orientation. Motivated by these atomistic observations, an original analytical model of inter-NW neck growth is formulated and validated. The model accurately predicts the unusual trends in neck growth with six orders of magnitude lesser computational effort than atomistic simulations. Further, it can handle nonisothermal temperature histories over millisecond time scales for NWs up to 100 nm in diameter, a capability that is beyond the reach of typical atomistic simulations. The impact of the revealed spatial disparity of nanoscale neck growth on the properties of random-packed NW assemblies, and the foundational role of the model in rational design and processing of printed multi-NW assemblies for a range of applications are discussed.

1. Introduction

The high electrical conductivity, desirable optical properties, resilience to deformation, and low-temperature fusion capability have made Ag NWs attractive for a range of flexible, conformal, and structural electronics.[1–4] A common and scalable processing route for such applications is to print NW inks, evaporate the solvent, and fuse the NWs, thus creating NW assemblies with desired electrical, optical, and mechanical properties. Inter-NW contacts in such NW assemblies occur primarily between vertically stacked NWs with nonorthogonal axes (**Figure 1**). Compared to chemical methods,[5] thermal fusion is more common for conductivity-limited applications since it often achieves higher conductivity and because recent developments have enabled scalable fusion even on thermally sensitive substrates.[6–9] Modeling neck growth between vertically stacked NWs is therefore crucial for rational design of NW geometry and control of NW printing and thermal fusion.

In situ microscopy during cold-welding of metal NWs provided unique insight into the nanoscale interaction between NWs in both end-to-end and side-to-side configurations[10] showing that welding can be performed at room temperature and with low forces. A subsequent follow-up work using molecular dynamics simulations was used to understand the mechanisms of such welding in detail.[11] We refer to cold welding as fusion at room temperature, to avoid confusion with the appreciable solid-state sintering that occurs well below the melting point of particles but above room temperature. Measurement of local electrical conductivity may be used as an indirect measure of neck growth but cannot resolve the neck growth at individual NW contacts.[12]

Current models that predict optical properties and electrical conductivity of NW assemblies only perform limited empirical modeling of how temperature affects these properties, since the explicit role of temperature history on fusion is ignored.[13,14] Cellular automata, Monte Carlo, phase field, and discrete element methods may potentially be used to model neck growth in NW assemblies.[15–18] There is no work on modeling NW fusion using the first three methods, likely because the need for significant domain discretization significantly increases the computational cost. The discrete element method does not suffer from this issue since discretization of the entire domain is not needed.[19] However, the discrete element method is driven by computationally rapid models of interparticle neck growth that are currently unavailable for NWs.

Molecular dynamics (MD) simulations have been widely used to mechanistically understand nanoparticle fusion.[20–22] Existing MD models of NW fusion are either confined to end-to-end or edge-to-edge NWs with parallel axes,[11,23,24] or are limited to

H. Devaraj, M. N. Jahangir, Dr. R. Malhotra
Mechanical and Aerospace Engineering
Rutgers University
Piscataway, NJ 08854, USA
E-mail: rajiv.malhotra@rutgers.edu
Z. Gao, Dr. C.-H. Chang
Chemical, Biological and Environmental Engineering
Oregon State University
Corvallis, OR 97331, USA

The ORCID identification number(s) for the author(s) of this article can be found under https://doi.org/10.1002/adts.202100104

DOI: 10.1002/adts.202100104

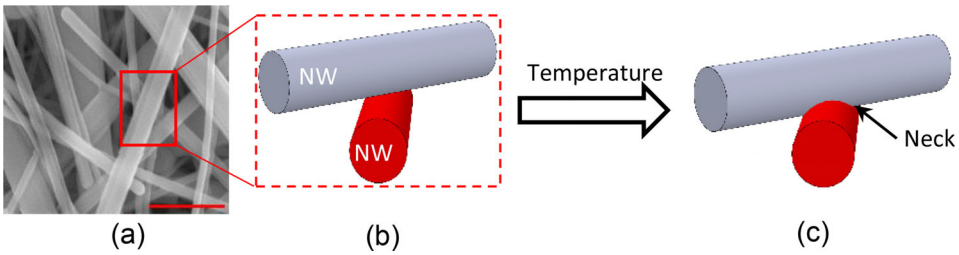

Figure 1. a) Micrograph of exemplar printed NW network. Reproduced with permission.[6] Copyright 2017, Royal Society of Chemistry. b,c) Inter-NW contact before and after fusion.

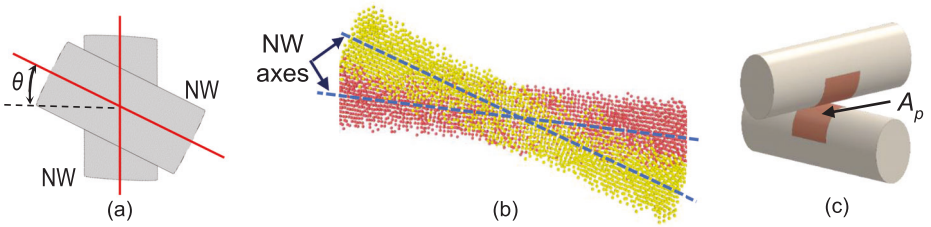

Figure 2. a) Schematic of orientation angle θ from top view. b) Snapshot of MD simulation from top view, for $R = 2.5$ nm and initial $\theta = 63°$. c) Schematic of projected area A_p.

orthogonal axes when dealing with vertically stacked NWs.[25,26] Generalizing results from such simulations to multi-NW assemblies assumes that the relative NW orientation does not change during fusion. This is equivalent to the assumption that relative NW orientation has no effect on fusion beyond a purely geometric one. As will be shown here, this assumption is only partially correct.

In summary, there is a lack of knowledge and of computationally efficient models of thermally driven fusion in device-relevant configurations (vertically stacked nonorthogonal NWs axes that are neither perpendicular nor parallel, Figure 1). This creates a major gap in the state-of-the-art in the context of printed electronics. We perform MD simulations to reveal a dynamic story of fusion in which surprisingly large NW rotation occurs as a nonlinear function of the initial NW orientation. The resulting nonlinear dependence of neck growth on initial orientation is explained based on the measured diffusion coefficients, dislocation density, and basic energetics principles. This knowledge is combined with conservation principles to derive an original analytical model of inter-NW neck growth, enabling computationally feasible fusion modeling over orders of magnitude larger time scales than MD. To retain clarity, we first discuss the method and insights for MD simulations and then the formulation and results of the analytical model.

2. Atomistic Model

2.1. Method

MD simulations were performed for the isothermal fusion of vertically stacked Ag NW pairs using the embedded atom method (EAM)[27] with potential functions from Mishin et al.[28] The fusion temperature was varied from 500 to 900 K, NW radius R from 2.5 to 7.5 nm, and initial orientation angle θ from 0° to 63° (**Figure 2**a). Each NW was 30 nm long and the total simulation time was 400 ps, during which the leveling off in potential energy indicated a leveling off in neck growth (Figures S1–S3, Supporting Information). The observed dependence of potential energy on temperature and NW radius agreed with the expected fusion-induced surface energy reduction. This MD model was validated against experimentally measured melting points in our previous work.[26]

The grain boundary and surface diffusion coefficients (D_b and D_s respectively) were computed using Einstein's relationship.[29] NW rotation was measured based on atomic positions on the NW axes. Note that the atomic displacements used to compute the diffusion coefficients were obtained by subtracting the displacement component due to NW rotation, in order to eliminate any nonphysical increase in diffusion coefficients due to large NW rotation. Dislocations created during fusion and the corresponding dislocation density D_d were computed based on the dislocation extraction algorithm developed by Stukowski.[30] The neck area A_n was measured as the planar area at the mid-section of the inter-NW neck.[24] This use of A_n rather than the typical use of neck radius is necessary in order to incorporate the high anisotropy in inter-NW neck size.[6,26] Nanoparticle fusion is often described in terms of the ratio of neck size to particle radius, a ratio that is commonly used to model properties such as electrical conductivity.[6,31]

We use an analogous regularized neck area ζ which is defined as the ratio of A_n to the projected area A_p. The A_p is defined as the area of the projection from the surface of one NW to the surface of the other (Figure 2c). This definition incorporates the effect of NW radius in a manner similar to that of the nanosphere radius in literature, but additionally includes the effect of initial θ (Table S1, Supporting Information). Further details on the MD model and on the computation of the above metrics are provided in the Supporting Information.

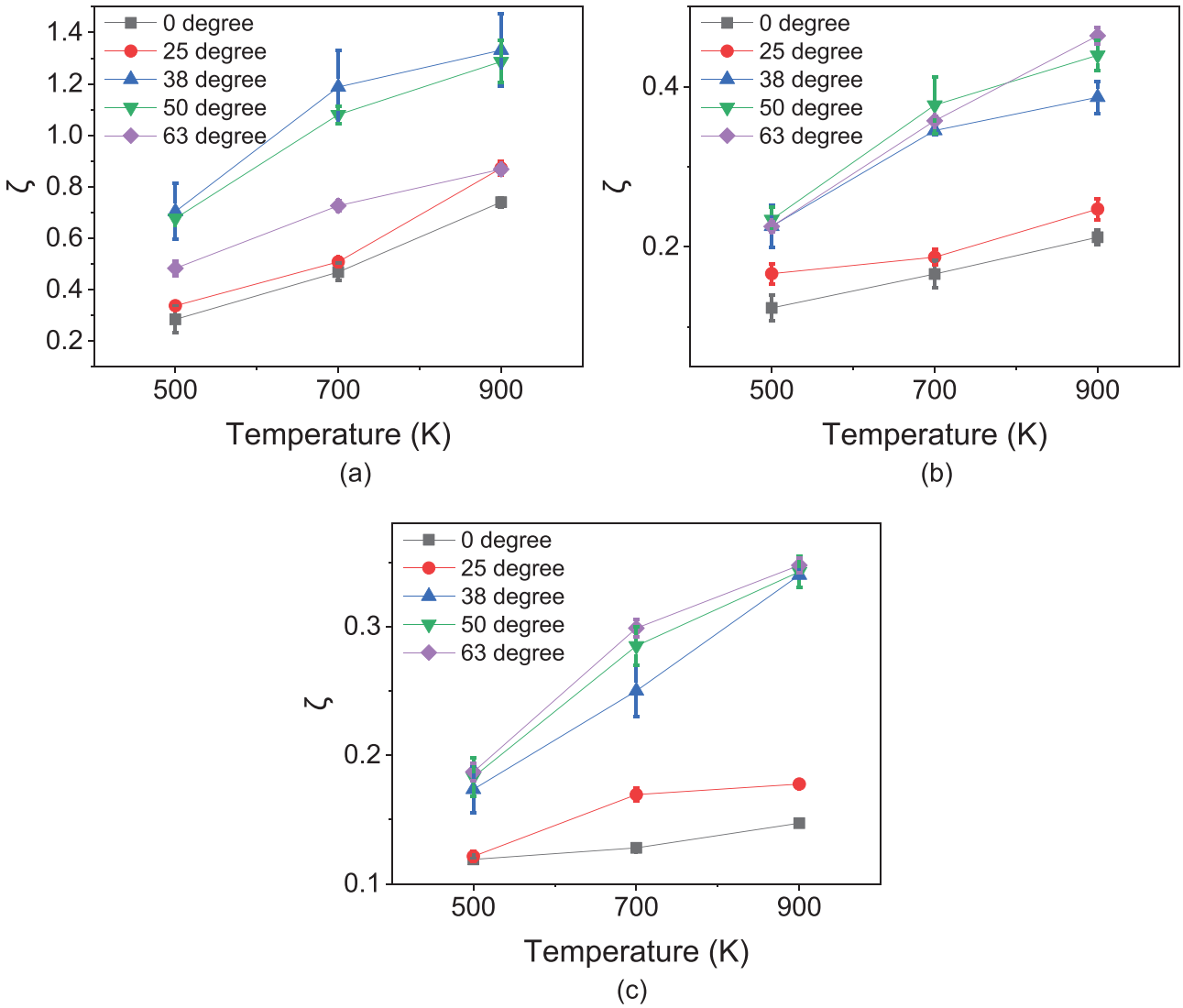

Figure 3. Dependence of ζ on temperature and initial θ for NW radius R = a) 2.5 nm, b) 5 nm, c) 7.5 nm.

2.2. Results

The increase in ζ with smaller radius and higher temperature (**Figure 3**) is as expected from fundamental considerations of size effects and thermal energy effects.[24,32] The ζ or regularized neck area is the ratio of the neck area to the area of the projection from the surface of one NW to the surface of the other (Figure 2c). The effect of the initial θ on the ζ, at the same temperature and radius, is much more interesting. When initial $\theta < 38°$ the initial NW orientation has a negligible effect on neck growth. The ζ suddenly increases for initial $\theta = 38°$. When the initial $\theta > 38°$ the ζ reduces for $R = 2.5$ nm and levels off for the larger NW radii. This reduction or leveling off in ζ for $R = 2.5$ nm is an artifact of the formulation of ζ and specifically of A_p, since the neck area A_n itself increases only very slightly for initial $\theta > 38°$ at this NW radius (Figure S4, Supporting Information). A multi-NW network typically contains many randomly aligned NW junctions. Thus, the above observations imply that even at the same fusion temperature we should expect significant junction-to-junction variation in neck growth within NW networks.

A crucial question is, why does the initial θ nonlinearly affect ζ ? From a purely geometric point-of-view higher initial θ means that more atoms along the NW axis can interact with each other, which in turn drives greater inter-NW diffusion. One can take this as a simple answer to our first question. The following analysis shows that this answer, which is based on the assumption that the NWs do not rotate during fusion, substantially underestimates the complexity and dynamic nature of NW fusion.

We analyze insights from atomic motion during MD. Since D_s (**Figure 4**) is much greater than D_b (Figure S5, Supporting Information), surface diffusion has a more dominant impact on neck growth than grain boundary diffusion. The jump in ζ for initial $\theta = 38°$ corresponds to a significant increase in D_s, which is in turn explained by an unexpectedly large NW rotation that tries to align the NW axes during fusion (**Figures 5 and 6** and Figures S6-S8, Supporting Information). This alignment forces

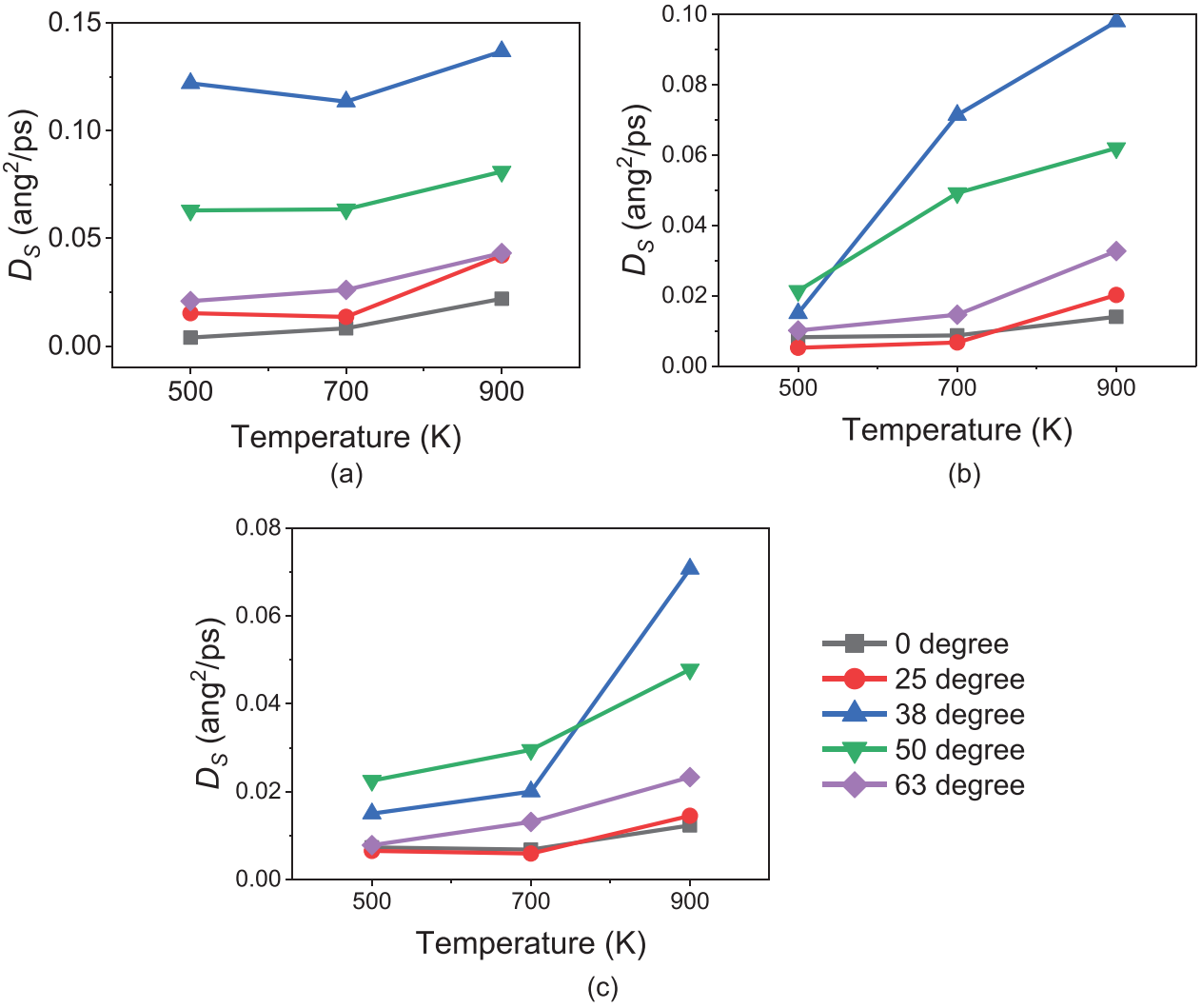

Figure 4. Surface diffusion coefficient D_s for NW radius R = a) 2.5 nm, b) 5 nm, c) 7.5 nm.

a larger number of atoms along the NW axes to interact with each other. Thus, NW-rotation-driven increase in surface diffusion is culpable for the observed neck growth trends when initial $\theta \leq 38°$.

Past experiments on cold welding of NWs have shown an "oriented attachment" mechanism in which fusion is easiest and fastest between NWs that have similar crystal orientations.[10] This indicates that in our stacked configuration aligned NW axes with the least dissimilarity in crystal orientations form a low-energy stable configuration that will be preferred if enough external energy is supplied to drive the system towards this minimum. Thus, mismatched crystal orientations between adjacent NWs can result in large NW rotation to reach this stable low-energy configuration if enough external energy is supplied. For the temperature-driven fusion process discussed here, this external energy is thermal in nature. As in experiments, the alignment of the NW axes with the <110> crystal orientation in our MD simulations creates a mismatch in crystal orientation between the NWs. Thus, NW rotation during fusion is in turn driven by an initial mismatch in the crystal orientation due to initial misalignment.

The above trends change for initial $\theta > 38°$. For 2.5 nm NW radius the D_s at initial $\theta = 50°$ is nearly half of that at 38° (Figure 4a) even though the ζ is very similar (Figure 3a) and neck growth is slightly greater (Figure S4a, Supporting Information). For 5 and 7.5 nm NW radii the D_s reduces significantly for initial $\theta > 38°$, but the corresponding change in ζ is insignificant and the magnitude of neck area actually increases (Figure S4b,c, Supporting Information). NW rotation is also much lesser in this zone of initial θ (Figure 6d,e). However, greater initial alignment between the NWs due to greater initial θ should result in greater diffusion because more atoms along the NW axes can interact. As discussed above, the observed D_s shows a contrary trend. Thus, rotation-driven or initial-alignment-driven diffusion cannot explain the trends in ζ when initial $\theta > 38°$.

The resolution to this conundrum is provided by the observation of edge and screw dislocations at the NW interface during fusion, as shown in **Figure 7** and Figures S9 and S10 (Supporting

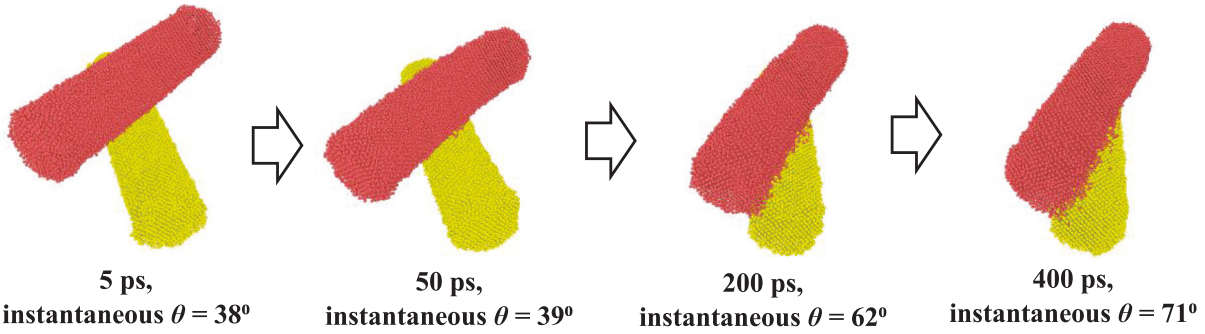

Figure 5. MD snapshots showing NW rotation for $R = 2.5$ nm and initial $\theta = 38°$ at 500 K temperature.

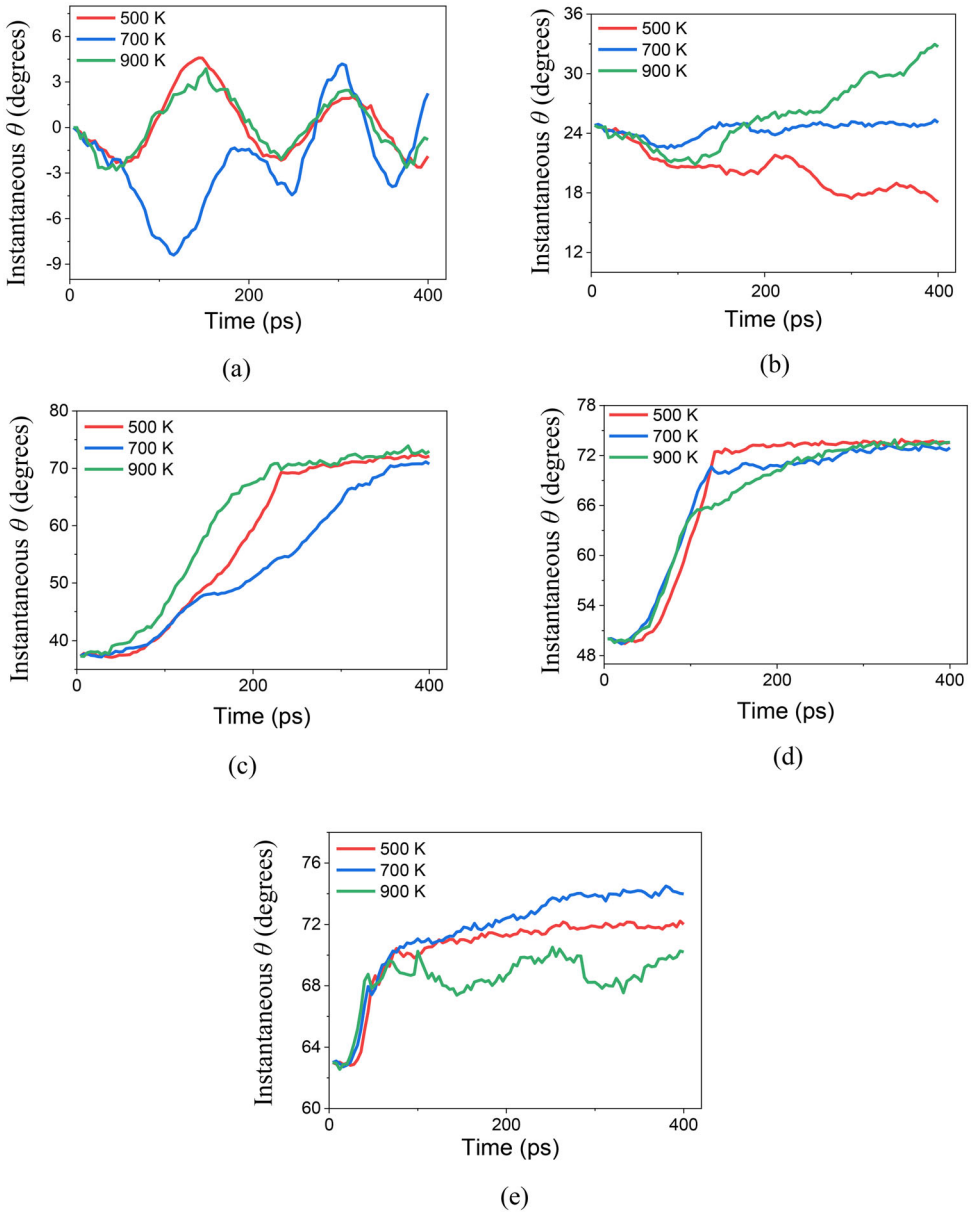

Figure 6. Evolution of θ for $R = 2.5$ nm and initial θ = a) 0°, b) 25°, c) 38°, d) 50°, e) 63°.

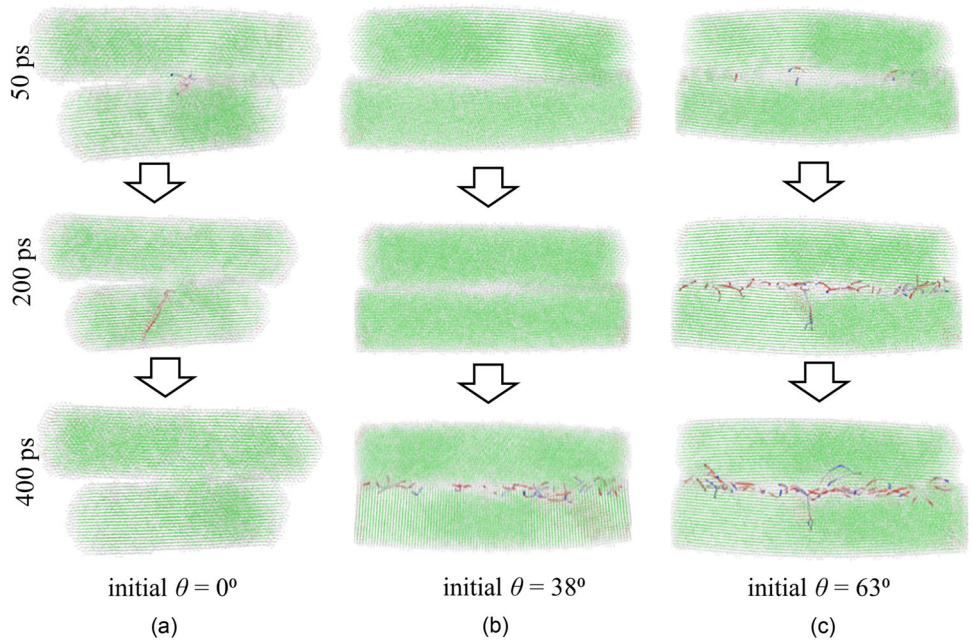

Figure 7. MD snapshots of dislocation generation for $R = 2.5$ nm at different initial θ. The red and blue lines are screw and edge dislocations and green points are Ag atoms.

Information). Such dislocation generation occurs because amorphous surface atoms at the NW interface try to recrystallize into the bulk crystal structure of Ag. When initial $\theta > 38°$, the dislocation density D_d increases with greater initial θ (**Figure 8** and Figures S11 and S12, Supporting Information). This, in turn, increases the dislocation-associated stress energy and encourages plasticity-driven neck growth.[21,33] Thus for initial $\theta > 38°$, it is greater dislocation generation that ensures enough neck growth despite a drastic reduction in the surface diffusion.

We observe that at initial $\theta = 38°$ there is a drastic jump in D_d around the 200 ps mark (Figure 8c). Further, a subsequent leveling off in D_d at a non-zero value indicates the creation of stable dislocations. While a similar trend is seen for initial $\theta > 38°$, the jump in D_d occurs significantly earlier during fusion. It is noteworthy that the dependence of rotation and D_d on the initial θ is quite similar and for initial $\theta \geq 38°$ the timing of the jump in D_d is very close to that at which NW rotation levels off.

These observations lead us to a comprehensive mechanism of neck growth for initial $\theta > 38°$. At low initial θ within this regime, NW rotation causes greater surface diffusion and reduces the system's surface energy. This rotation also encourages greater contact between the NW surfaces which drives more surface recrystallization, dislocation creation, and plasticity-driven neck growth, albeit contributing to a lesser extent to fusion than surface diffusion. As the initial θ increases in this regime, greater NW prealignment creates more opportunities for recrystallization even without NW rotation, as evidenced by the earlier jump in D_d. Thus, dislocation-driven neck growth begins to dominate at larger orientation angles by creating an alternate route to surface energy reduction than surface diffusion. As a result, the surface diffusion starts to reduce beyond the critical initial θ of 38°.

We now describe a holistic energy-based view of inter-NW neck growth across the entire range of initial θ. NW rotation enables higher reduction in surface energy of the system during fusion since it allows more atoms along the NW axes to interact. However, this requires the external thermal energy to surmount the energy barrier (or work needed) for rotation. When the initial θ is too low (0°–25°) then the external thermal energy cannot overcome this barrier and NW rotation is negligible. Beyond a certain NW prealignment (initial $\theta = 38°$ here) the rotation energy barrier is reduced enough that external thermal energy can overcome it. The resulting increase in NW rotation drives greater surface diffusion and neck growth than would be expected from purely geometric considerations. Greater atomic interaction due to NW rotation concurrently increases dislocation generation, which has a negative feedback effect on NW rotation via the creation of an alternative pathway for reduction of the system's surface energy. This is supported by the virtual stop in NW rotation as soon as there is a significant jump in D_d during fusion (Figures 6 and 8). As the initial θ increase beyond 38° there is a progressive increase in dislocation-driven neck growth, till it finally overwhelms surface diffusion. As a result, NW rotation reduces but neck growth is still significant.

3. Analytical Model

3.1. Method

We formulate an analytical model of inter-NW neck growth that is compatible with the discrete element method. This model builds on past work in which analytical equations are derived for neck growth between adjacent nanospheres based on free energy minimization and conservation principles.[34–36] However, these existing models ignore two crucial peculiarities of NW fusion. First, unlike the planar circular neck created during nanosphere fusion (**Figure 9**a) the neck formed at an inter-NW junction is a 3D

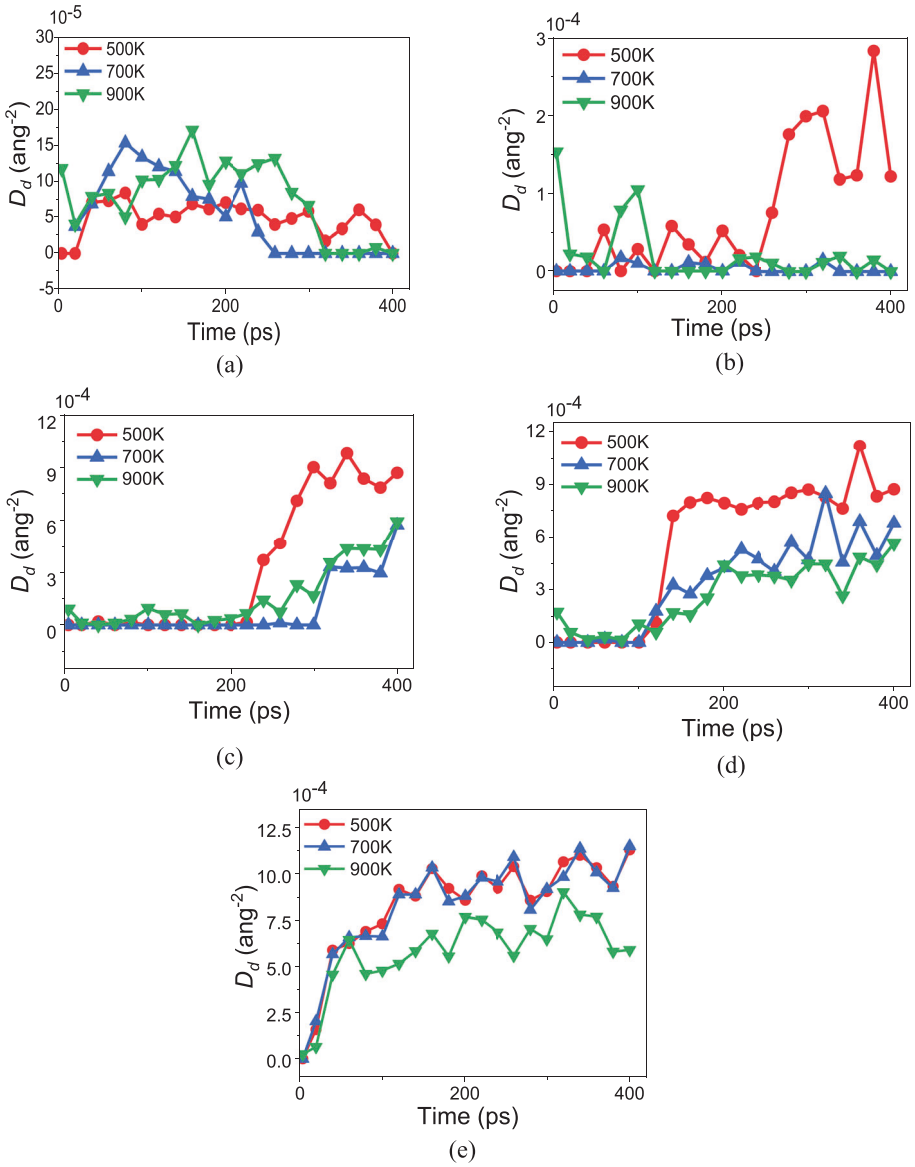

Figure 8. Evolution of dislocation density for $R = 2.5$ nm and initial θ = a) 0°, b) 25°, c) 38°, d) 50°, e) 63°.

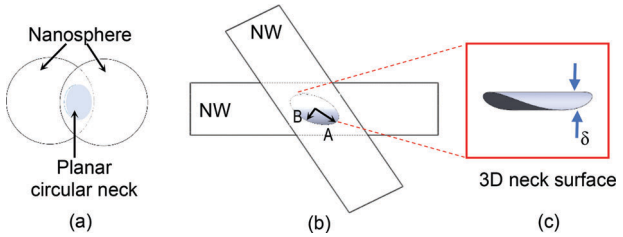

Figure 9. Neck geometry for a) nanospheres; and for NWs b) top view, and c) side view.

hyperbolic paraboloid (Figure 9b,c). Second, the NW rotation seen in the MD simulations cannot be incorporated into these existing models.

For simplicity we replace the multiple mechanisms of neck growth uncovered in MD simulations with one mechanism, i.e., a pseudo shrinkage δ (Figure 9c) due to grain boundary diffusion with a diffusion coefficient D_{eff}. We further assume that the specific surface energy γ_s and atomic mobility are isotropic along the neck boundary and the normal stress on the neck surface due to atomic diffusion is symmetric about the center of the neck.

The neck area measured in our MD simulations is an ellipse with A and B as the major and minor axes (Figure 9b). The dependence of A and B on radius R and on the instantaneous θ and δ is obtained geometrically, as described in the Supporting Information. However, using A and B directly for shrinkage computation would ignore the large neck curvature. We use a perturbation parameter $\epsilon = 0.11\delta/(A+B)$ to obtain an effective planar and elliptical neck surface with major axis a and minor axis b for

shrinkage calculations (Equations 1 and 2).[37,38] The value of the constant pre-multiplier for ϵ is obtained by geometrically equating the perimeter of the 3D neck to that of the effective planar neck. Updating θ and δ in a time-marching manner yields the evolution of the neck area.

$$a(\delta, \theta, R) = A(\delta, \theta, R) \cdot (1 + \varepsilon) \tag{1}$$

$$b(\delta, \theta, R) = B(\delta, \theta, R) \cdot (1 + \varepsilon) \tag{2}$$

Based on energy conservation the diffusive flux j is related to the normal stress σ on the neck boundary, diffusion coefficient D_{eff}, temperature T, atomic volume Ω (10.3 $\text{cm}^3\ \text{mol}^{-1}$ for Ag), and Boltzmann constant k, as shown in Equation 3.[35] The σ is also proportional to the principal curvature K of the free neck surface and the specific surface energy γ_s (1×10^{-18} J nm^{-2} for Ag), as shown in Equation 4.[35–36]

$$j = \frac{D_{\text{eff}}\Omega}{kT} \nabla\sigma \tag{3}$$

$$\sigma = \gamma_s K \tag{4}$$

Using the principle of mass conservation, as described in the Supporting Information, the K is empirically found to be $\approx 1/\delta$ for NW radii up to 500 nm. The normal force driving shrinkage is obtained as the integral of the normal stress over the neck area. This force equals the surface tension force on the neck boundary.[34,35] The assumption of isotropic mass flow within the neck surface means that the divergence of the diffusive flux is constant. Using these insights along with the flux equation, the symmetric stress condition at the center of the neck, and the mass conservation principle yields the shrinkage rate expression in Equation 5 (see Supporting information for detailed derivation). Here, P is the perimeter factor of the effective planar ellipse and ψ is the dihedral angle (assumed constant $\approx 70°$).[34]

$$\dot{\delta} = \frac{D_{\text{eff}}\Omega}{kT} \frac{P}{\sqrt{ab}} \frac{4\gamma_s}{ab} \cdot \left[2K - \frac{P}{ab}\sin(\psi)\right] \tag{5}$$

$$\dot{\theta} = \frac{\Gamma}{\eta\pi\ (a^2 b^2)} \tag{6}$$

We treat the evolution of θ as a consequence of a virtual torque Γ applied to the neck. Based on the conservation of angular momentum, and denoting a corresponding rotational drag coefficient as η (1×10^{-11} kg nm^{-2} s[36,39]), the rate form of the rotation is shown in Equation 6. A detailed derivation is omitted here but is provided in the supporting information. Using the principle of momentum conservation,[40] the above expressions for shrinkage rate and rotation rate yield Equation 7 for a NW pair (NWs denoted by superscripts 1 and 2).

$$\begin{bmatrix} \frac{\pi}{4}\frac{kT}{D_{\text{eff}}\Omega}\frac{ab\sqrt{ab}}{P} & 0 & -\frac{\pi}{4}\frac{kT}{D_{\text{eff}}\Omega}\frac{ab\sqrt{ab}}{P} & 0 \\ 0 & \eta_c\pi\ ab\sqrt{ab} & 0 & -\eta_c\pi\ ab\sqrt{ab} \\ -\frac{\pi}{4}\frac{kT}{D_{\text{eff}}\Omega}\frac{ab\sqrt{ab}}{P} & 0 & \frac{\pi}{4}\frac{kT}{D_{\text{eff}}\Omega}\frac{ab\sqrt{ab}}{P} & 0 \\ 0 & -\eta_c\pi\ ab\sqrt{ab} & 0 & \eta_c\pi\ ab\sqrt{ab} \end{bmatrix} \times \begin{bmatrix} \dot{\delta}^{(1)} \\ \dot{\theta}_t^{(1)} \\ \dot{\delta}^{(2)} \\ \dot{\theta}_t^{(2)} \end{bmatrix} = \begin{bmatrix} \pi\gamma_s\left[2K - \frac{P}{ab}\sin(\psi)\right] \\ \pi\Gamma/\sqrt{ab} \\ -\pi\gamma_s\left[2K - \frac{P}{ab}\sin(\psi)\right] \\ -\pi\Gamma/\sqrt{ab} \end{bmatrix} \tag{7}$$

The functional forms of D_{eff} and Γ are formulated and calibrated against observations from MD simulations. The dominant diffusion coefficient (D_s) measured from MD has an Arrhenius dependence on temperature T and a dependence on the initial θ as shown in **Figure 10**a, Figures S13a and S14a (Supporting Information). D_{eff} is modeled as a normal gaussian function of the instantaneous θ and as an Arrhenius function of temperature T (Equation 8). R_g is the universal gas constant. To capture the effect of NW radius, the pre-exponential factor D_0 and the activation energy E_a are cast as functions of R (Equations S19 and S20, Supporting Information). Further, the standard deviation σ_D is a function of T (Equation S17, Supporting Information).

$$D_{\text{eff}} = \frac{D_o . e^{\left(\frac{-E_a}{R_g}\cdot\frac{1}{T}\right)}}{2\pi\sigma_D} . e^{\left(\frac{-(\theta-45)^2}{2\sigma_D{}^2}\right)} \tag{8}$$

$$\Gamma = \frac{g\left(R, T, \theta_0\right)}{2\pi\sigma_\Gamma} . e^{\left(\frac{-(\theta-45)^2}{2\sigma_\Gamma{}^2}\right)} \tag{9}$$

The torque Γ is measured from MD simulations based on the observation that $\Gamma = 2I\Delta\theta/t_f^2$, where I is the moment of inertia of the NW pair about the rotation axis and $\Delta\theta$ is the change in angle θ measured from MD over the fusion time $t_f = 400$ ps. Given the dependence of Γ on initial θ (Figure 10b and Figures S13a and S14a, Supporting Information) the dependence of Γ on the instantaneous θ was modeled as a normal Gaussian function as shown in Equation 9. The function g is cast a function of R, T, and the initial angle θ_0 (Equations S21–S23, Supporting Information). The form and parameters of the functions D_0, E_a, σ_D, g, and σ_T were manually calibrated by matching the neck area predicted by the analytical model to that from MD. The calibrated formulations for these functions are shown in the Supporting Information. The analytical simulation began with a small initial shrinkage of $0.08R$ to prevent computational issues.

3.2. Results

Figure 11 shows good agreement between the neck growth predictions from MD and the analytical model for the calibration cases, indicating good calibration of our analytical model from MD observations. Our model was validated by comparing neck area prediction to MD simulations for NW radii, fusion temperatures, initial orientations, and fusion time, beyond that in the calibration dataset. First, we examined the effect of using initial angles and fusion temperatures other than those used for calibration. We performed MD and analytical simulations over a simulation time of 400 ps for $R = 2.5$ nm at initial angle 15° at temperature 450 K, for $R = 5$ nm at initial angle 45° at temperature 400 K, and for $R = 7.5$ nm at initial angle 70° at temperature 600 K. As shown in **Figure 12**a the neck area predictions are accurate even

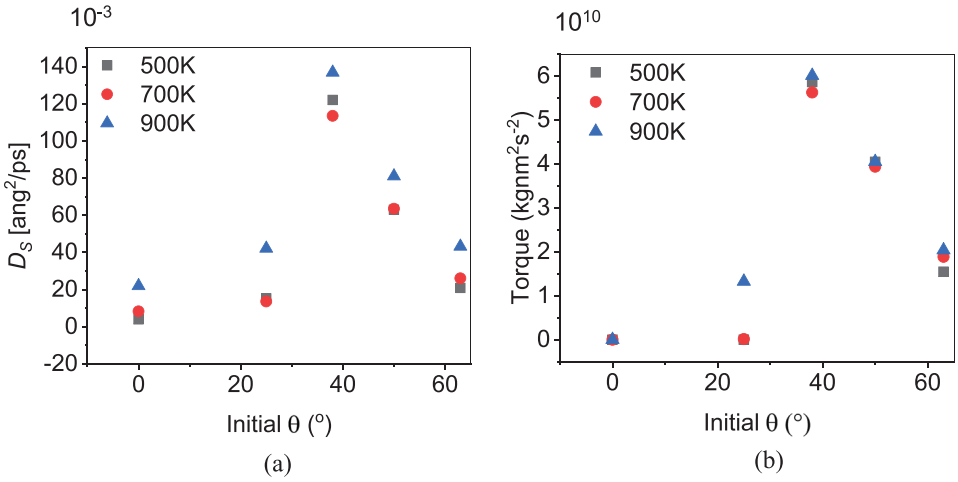

Figure 10. Effect of initial θ on a) surface diffusion coefficient, b) effective torque from MD after 400 ps of fusion time for $R = 2.5$ nm.

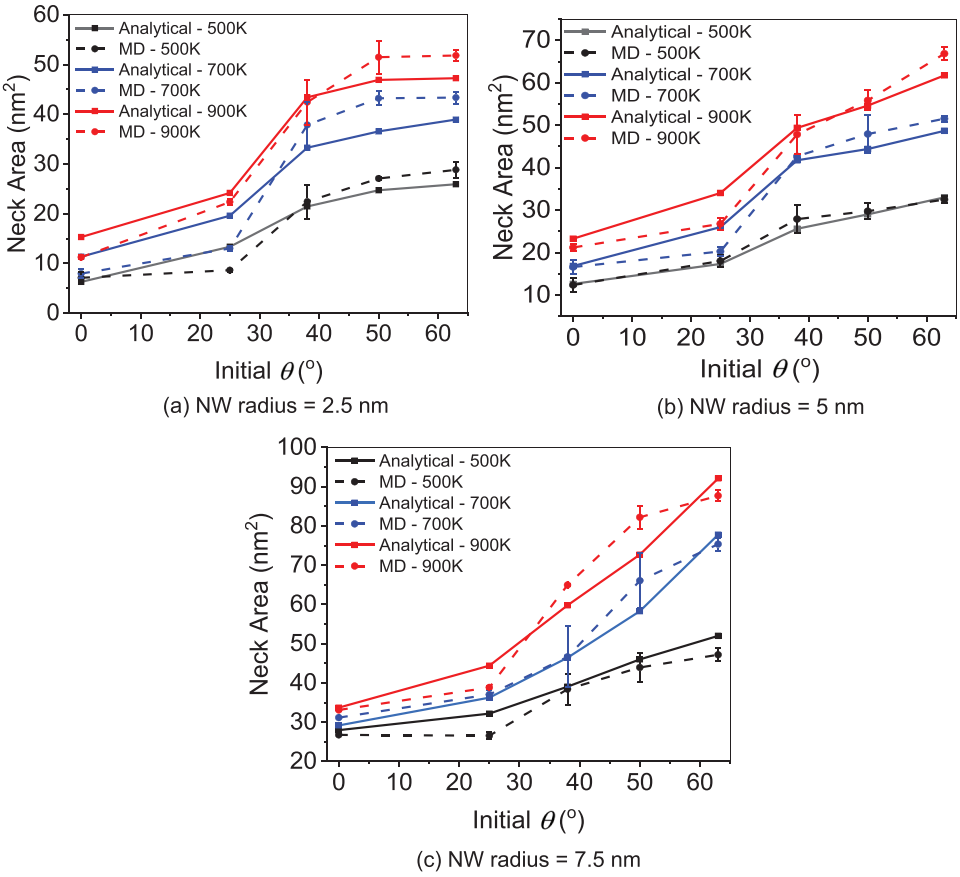

Figure 11. Neck area comparison between the calibrated analytical model and corresponding MD simulations for NW radii of a) 2.5 nm, b) 5 nm, c) 7.5 nm.

for initial angles and thermal histories that were not used for calibration.

Next, the applicability of the analytical model to NW radii and fusion time beyond that used for calibration was examined. Predictions from MD and analytical simulations were compared for a constant initial angle of 45° and temperature 450 K for the cases of $R = 10$ nm up to a fusion time of 400 ps, $R = 12.5$ nm up to a fusion time of 208 ps and $R = 15$ nm up to a fusion time of 102 ps. A shown in Figure 12b, our analytical model is valid well beyond the maximum NW radii used for model calibration. The computational effort for our analytical model is orders of magnitude lesser than that for MD simulations. For example, a MD

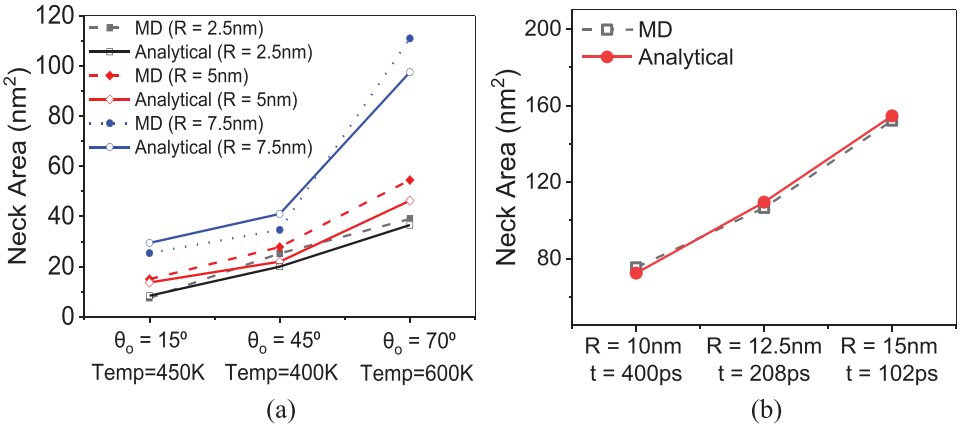

Figure 12. Validation of analytical model against MD simulations for a) varying R, initial angle θ_0 & temperature, for a fusion time of 400 ps, b) varying R beyond the range of radii used for calibration, at 450 K fusion temperature and initial $\theta = 45°$.

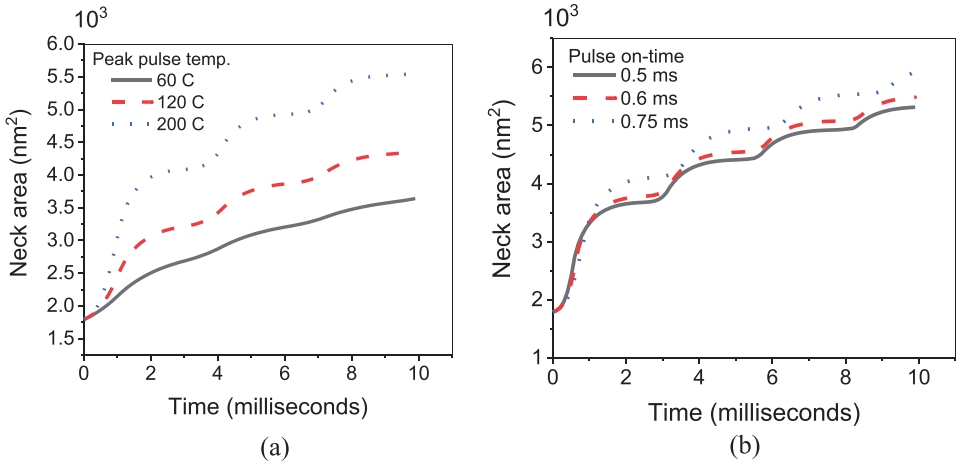

Figure 13. Neck area predictions from analytical model for triangular temperature pulses. a) Effect of peak temperature for 50 nm NW radius, initial $\theta = 45°$, pulse on-time = 1 ms, pulse off-time = 2 ms, number of pulses = 4; b) effect of pulse on-time for 50 nm NW radius, initial $\theta = 45°$, pulse off-time = 2 ms, number of pulses = 4, peak pulse temperature = 200 °C. Lowest pulse temperature = 25 °C.

simulation for initial $\theta = 38°$ requires 48 h using a 64 processor workstation but only 0.75 s on a 7 processor laptop using our analytical model. This is equivalent to $\approx 3 \times 10^3$ CPU hours for MD simulations and $\approx 1.5 \times 10^{-3}$ CPU hours for the analytical model, six orders of magnitude improvement in computational effort. Based on past work on phase-field modeling,[15–17] Monte Carlo simulations,[41] and cellular automata simulations[18] the computational effort of our model should still be lesser by a few orders of magnitude, although this needs to be tested by modeling NW fusion using these methods.

We further examine the ability of our analytical model to handle nonisothermal temperature histories that are relevant to emerging scalable fusion processes such as laser and intense pulsed light fusion.[9,25,26,42] **Figure 13** shows predictions of neck growth from our model for 100 nm NW diameter, for a series of triangular temperature pulses spanning milliseconds of fusion time. The effect of the peak pulse temperature and the pulse on-time is examined and the details of the initial orientation angles and of the pulse and temperature variation during the pulse are shown in the caption of Figure 13. The predicted dependence of neck growth on the peak pulse temperature and on the pulse on-time qualitatively agrees with experiments from past work in the above processes. Thus, our analytical model can access complex temperature histories over time and length scales that are typically beyond the reach of typical MD simulations. We further observe that for this size of NWs the rotation was predicted to be negligible, indicating that the role of rotation reduces as the NW diameter increases. Physically, this makes sense because NWs with larger diameters have greater inertia and therefore need more energy to rotate.

4. Conclusion

The main contributions of this paper are as follows. During fusion of vertically stacked NWs, there is significant recrystallization-driven local rotation perpendicular to the NW axes, This accelerates surface diffusion and dislocation-driven plasticity as avenues for inter-NW neck growth, with each

mechanism dominant in regimes demarcated by the initial NW orientation. The cumulative effect is to increase neck growth beyond that possible from a purely geometric point-of-view. We note that in a multi-NW assembly this rotation is likely local in nature, given the constraining effect of neck growth at multiple junctions along the length of a NW. Our finding implies that the local NW orientation in a multi-NW assembly has a significantly stronger influence on local neck growth; and therefore, on the electrical, optical and mechanical properties of the assembly; than previously imagined.

Our novel analytical model captures the above peculiarities of NW fusion, but goes significantly beyond the length and time scale limitations of MD simulations. Within our knowledge, this is the first analytical model that can quantitatively predict neck growth during NW fusion for realistic NW configurations. Our model incorporates the 3D shape of the neck and NW rotation, idiosyncrasies of NW fusion that constitute a major departure from conventional fusion models. Our model requires 6 orders of magnitude lesser computational effort than MD, can handle complex non-isothermal temperature histories, and can access NW diameters and fusion times well beyond the reach of MD simulations. Combining these qualities creates a pathway to the rational design of NW geometry and the printing and fusion parameters while the compatibility with the scalable Discrete Element Method (via Equation 7) will allow eventual incorporation of the coupling between neck growth at adjacent NW junctions in large NW ensembles. Realizing this potential to control process-structure–property relationships for random packed multi-NW assemblies is an ongoing effort in our research group.

Supporting Information

Supporting Information is available from the Wiley Online Library or from the author.

Acknowledgements

This work was supported by the National Science Foundation, USA, grants CMMI # 2001081, CMMI #1809289, and CBET # 1449383.

Conflict of Interest

The authors declare no conflict of interest.

Data Availability Statement

Research data are not shared.

Keywords

analytical models, molecular dynamics, nanowires, scalable fusion

Received: March 24, 2021
Revised: May 30, 2021
Published online: July 11, 2021

[1] A. Teymouri, E. Adabifiroozjaei, R. F. Webster, S. M. Hagh, X. Hao, M. A. Green, S. Pillai, *ACS Appl. Nano Mater.* **2020**, *3*, 3205.
[2] W. Xu, L. Zhong, F. Xu, W. Shen, W. Song, S. Chou, *ACS Appl. Nano Mater.* **2018**, *1*, 3859.
[3] B. Zhou, Q. Li, P. Xu, Y. Feng, J. Ma, C. Liu, C. Shen, *Nanoscale* **2021**, *13*, 2378.
[4] S. Huang, C. Feng, E. L. H. Mayes, B. Yao, Z. He, S. Asadi, T. Alan, J. Yang, *Nanoscale* **2020**, *12*, 19861.
[5] Y. Kim, Y. E. Sul, H. Kang, Y. Choi, H. S. Lim, S. Lee, L. Pu, G.-R. Yi, S. M. Cho, J. H. Cho, *Nanoscale* **2018**, *10*, 18627.
[6] M. Dexter, R. Bhandari, C. Chang, R. Malhotra, *RSC Adv.* **2017**, *7*, 56395.
[7] C. Wan-Ho, H. Yeon-Taek, L. Seung-Hyun, K. Hak-Sung, *Nanotechnology* **2016**, *27*, 205704.
[8] M. N. Jahangir, J. Cleeman, H.-J. Hwang, R. Malhotra, *Addit. Manuf.* **2019**, *30*, 100886.
[9] H. Devaraj, H.-J. Hwang, R. Malhotra, *J. Manuf. Processes* **2020**, *58*, 1088.
[10] Y. Lu, J. Y. Huang, C. Wang, S. Sun, J. Lou, *Nat. Nanotechnol.* **2010**, *5*, 218.
[11] Z. S. Pereira, E. Z. da Silva, *J. Phys. Chem. C* **2011**, *115*, 22870.
[12] G. Milano, A. Cultrera, K. Bejtka, N. De Leo, L. Callegaro, C. Ricciardi, L. Boarino, *ACS Appl. Nano Mater.* **2020**, *3*, 11987.
[13] D. P. Langley, M. Lagrange, G. Giusti, C. Jiménez, Y. Bréchet, N. D. Nguyen, D. Bellet, *Nanoscale* **2014**, *6*, 13535.
[14] M. Lagrange, D. P. Langley, G. Giusti, C. Jiménez, Y. Bréchet, D. Bellet, *Nanoscale* **2015**, *7*, 17410.
[15] Y. Yang, O. Ragnvaldsen, Y. Bai, M. Yi, B.-X. Xu, *npj Comput. Mater.* **2019**, *5*, 81.
[16] O. G. Dibua, A. Yuksel, N. K. Roy, C. S. Foong, M. Cullinan, *J. Micro Nano-Manuf.* **2018**, *6*, 041004.
[17] F. Abdeljawad, D. S. Bolintineanu, A. Cook, H. Brown-Shaklee, C. DiAntonio, D. Kammler, A. Roach, *Acta Mater.* **2019**, *169*, 60.
[18] W. Tan, N. S. Bailey, Y. C. Shin, *Comput. Mater. Sci.* **2011**, *50*, 2573.
[19] R. Castro, in *Sintering: Mechanisms of Convention Nanodensification and Field Assisted Processes*, Vol. *1* (Eds: H. R. C. Ricardo, K. van Benthem), Springer, New York **2013**, pp. 17–34.
[20] S. Yang, W. Kim, M. Cho, *Int. J. Eng. Sci.* **2018**, *123*, 1.
[21] J. Wang, S. Shin, A. Hu, *J. Phys. Chem. C* **2016**, *120*, 17791.
[22] J. Xu, Y. Higuchi, N. Ozawa, K. Sato, T. Hashida, M. Kubo, *ACS Appl. Mater. Interfaces* **2017**, *9*, 31816.
[23] G. Okeke, S. J. Antony, R. B. Hammond, K. Ahmed, *J. Nanopart. Res.* **2017**, *19*, 237.
[24] Z. Wu, X. Yang, Z. Wang, *Nanotechnology* **2019**, *30*, 245601.
[25] M. Dexter, A. Pfau, Z. Gao, G. S. Herman, C.-h. Chang, R. Malhotra, *Nanotechnology* **2018**, *29*, 505205.
[26] H.-J. Hwang, R. Malhotra, *ACS Appl. Mater.* **2018**, *11*, 3536.
[27] M. S. Daw, M. I. Baskes, *Phys. Rev. B* **1984**, *29*, 6443.
[28] Y. Mishin, D. Farkas, M. Mehl, D. Papaconstantopoulos, *Phys. Rev. B* **1999**, *59*, 3393.
[29] D. J. Keffer, P. Adhangale, *Chem. Eng. J.* **2004**, *100*, 51.
[30] A. Stukowski, V. V. Bulatov, A. J. M. Arsenlis, *Modell. Simul. Mater. Sci. Eng.* **2012**, *20*, 085007.
[31] W. MacNeill, C.-H. Choi, C.-H. Chang, R. Malhotra, *Sci. Rep.* **2015**, *5*, 14845.
[32] M. Jose-Yacaman, C. Gutierrez-Wing, M. Miki, D.-Q. Yang, K. Piyakis, E. Sacher, *J. Phys. Chem. B* **2005**, *109*, 9703.
[33] F. Wang, Z. Tang, H. He, *AIP Adv.* **2018**, *8*, 045012.
[34] R. Castro, K. Benthem, *Sintering: Mechanisms of Convention Nanodensification and Field Assisted Processes*, Springer, New York **2013**.

[35] D. L. Johnson, *J. Appl. Phys.* **1969**, *40*, 192.
[36] F. Parhami, R. M. McMeeking, *Mech. Mater.* **1998**, *27*, 111.
[37] L. Jiji, *Heat Conduction*, Springer, New York **2009**.
[38] *Nature* **1965**, *206*, 226.
[39] F. B. Swinkels, M. F. Ashby, *Acta Metall.* **1981**, *29*, 259.
[40] F. Parhami, R. M. McMeeking, A. C. F. Cocks, Z. Suo, *Mech. Mater.* **1999**, *31*, 43.
[41] K. C. Lai, J. W. Evans, D.-J. Liu, *J. Chem. Phys.* **2017**, *147*, 201101.
[42] A. J. Lopes, I. H. Lee, E. MacDonald, R. Quintana, R. Wicker, *J. Mater. Process. Technol.* **2014**, *214*, 1935.